THE JOURNAL OF BIOLOGICAL CHEMISTRY VOL. 290, NO. 32, pp. 19569–19583, August 7, 2015

Structural Characterization of Bardet-Biedl Syndrome 9 Protein (BBS9)*

Received for publication, March 2, 2015, and in revised form, June 1, 2015 Published, JBC Papers in Press, June 17, 2015, DOI 10.1074/jbc.M115.649202

Kevin E. Knockenhauer and Thomas U. Schwartz[1]

From the Department of Biology, Massachusetts Institute of Technology, Cambridge, Massachusetts 02139

Background: BBS9 is a component of the octameric BBSome, a complex that transports membrane proteins to the primary cilium.
Results: BBS9 has four folded domains, based on structure prediction; the N-terminal domain is a β-propeller.
Conclusion: BBS9 likely acts as a scaffold component in the BBSome coat.
Significance: The structural data help in understanding a mutation that causes Bardet-Biedl syndrome.

The Bardet-Biedl syndrome protein complex (BBSome) is an octameric complex that transports membrane proteins into the primary cilium signaling organelle in eukaryotes and is implicated in human disease. Here we have analyzed the 99-kDa human BBS9 protein, one of the eight BBSome components. The protein is composed of four structured domains, including a β-stranded N-terminal domain. The 1.8 Å crystal structure of the 46-kDa N-terminal domain reveals a seven-bladed β-propeller. A structure-based homology search suggests that it functions in protein-protein interactions. We show that the Bardet-Biedl syndrome-causing G141R mutation in BBS9 likely results in misfolding of the β-propeller. Although the C-terminal half of BBS9 dimerizes in solution, the N-terminal domain only does so in the crystal lattice. This C-terminal dimerization interface might be important for the assembly of the BBSome.

The primary cilium is a singular, microtubule-based protrusion from the plasma membrane found in nearly all vertebrate cell types. The microtubule bundle, termed the axoneme, forms the structural scaffold of this finger-like projection and is surrounded by the lipid bilayer except at its base, where it originates from the mother centriole in the cytoplasm (1). Unlike motile cilia, the role of the primary cilium is not locomotion but rather signal transduction and, as a consequence, is essential to Hedgehog and non-canonical Wnt signaling pathways (2). Despite being continuous with the plasma membrane, the membrane of the primary cilium has a unique composition of proteins, namely an enrichment of specific G-protein-coupled receptors involved in signaling (1, 3). How this organelle maintains the integrity and specificity of its compartment remains an active area of investigation, although a septin diffusion barrier has been shown to play a critical role (4, 5).

One such component to the establishment and maintenance of the unique protein composition of the ciliary membrane is the BBSome,[2] an immunoprecipitation-stable, eight-membered protein complex comprising BBS1, BBS2, BBS4, BBS5, BBS7, BBS8, BBS9, and BBIP10 (6, 7). The genes coding for seven of these proteins were originally identified based on their mutation in a rare, autosomal recessive genetic disorder termed Bardet-Biedl syndrome (BBS (8)). BBS is a pleiotropic disease characterized by mental retardation, polycystic kidneys, obesity, vision problems, and hypogonadism (1, 8). Evidence for BBSome function was seen in BBS2 and BBS4 knock-out mice, where a G-protein-coupled receptor resident of the ciliary membrane, somatostatin receptor type 3, fails to localize to the primary cilium in neurons (9). The BBSome has been shown to localize to the ciliary membrane and to coat liposomes in an Arl6-GTP-dependent manner through thin section electron microscopy, leading to the hypothesis that the complex forms a membrane protein transport coat similar to COPI or COPII (10). Consistent with this hypothesis, proteins of the BBSome and the coat-forming elements of COPI, COPII, and clathrin share a similar domain composition and architecture (10): namely, N-terminal β-propeller and C-terminal appendage domains, as is the case for BBS1, BBS2, BBS7, and BBS9, and α-solenoid domains, as in BBS4 and BBS8 (10). Recently, an additional role of the BBSome in the assembly and recycling of intraflagellar transport particles, which move cargo along the axoneme via microtubule motors, has been identified through a loss-of-function mutation of BBS1 in *Caenorhabditis elegans* (11).

Given the structural homology to vesicle coat proteins on a domain level, we set out to assess whether and to what degree this homology held true on the atomic level. To this end, another group has already reported the first high-resolution crystal structure of a BBS protein, the BBS1 N-terminal β-propeller from *Chlamydomonas reinhardtii* in complex with the

* This work was supported by National Institutes of Health Grant T32GM007287 (to K. E. K.) and the National Science Foundation Graduate Research Fellowship under Grant 1122374 (to K. E. K.). The authors declare that they have no conflicts of interest with the contents of this article.
The atomic coordinates and structure factors (code 4YD8) have been deposited in the Protein Data Bank (http://wwpdb.org/).
[1] To whom correspondence should be addressed: Dept. of Biology, Massachusetts Institute of Technology, 77 Massachusetts Ave., Cambridge, MA 02139. Tel.: 617-452-3851; Fax: 617-258-6553; E-mail: tus@mit.edu.

[2] The abbreviations used are: BBSome, Bardet-Biedl syndrome protein complex; BBS9, Bardet-Biedl syndrome 9 protein; BBS, Bardet-Biedl syndrome; 3C, human rhinovirus 3C protease; SeMet, selenomethionine; NCS, noncrystallographic symmetry; MSA, multiple sequence alignment; SEC, size exclusion chromatography; AUC, analytic ultracentrifugation; RMSD, root mean square deviation; HsBBS9, *H. sapiens* BBS9; CrBBS1, *C. reinhardtii* BBS1; ScSUMO, *S. cerevisiae* small ubiquitin-like modifier.

Arl6-GTPase (12). Here we present the high-resolution crystal structure of the BBS9 N-terminal β-propeller from *Homo sapiens* and explain the structural basis of the G141R point mutation that causes BBS in humans (13). BBS9 knockdown in zebrafish leads to defects in ciliogenesis and neuronal development that the G141R mutant fails to rescue (14).

Experimental Procedures

Cloning—The *H. sapiens* BBS9 open reading frame was PCR-amplified with BamHI (5′) and NotI (3′) restriction site overhangs from cDNA (Open Biosystems) and subcloned into a modified pETDuet-1 vector, containing an N-terminal His_{10}-Arg_8-ScSUMO-3C cleavage site tag, via restriction digest. Subsequent inverse PCRs were performed on this vector to remove the coding region for either the N-terminal domain ($HsBBS9_{1-407}$) or the C-terminal half of the protein ($HsBBS9_{405-887}$). The resulting linearized vectors were recircularized by enzymatic treatment with T4 phosphonucleotide kinase (New England Biolabs) and T4 ligase (New England Biolabs). $HsBBS9_{1-407}$ G141R and all other point mutations were generated via site-directed mutagenesis.

Protein Expression and Purification—LOBSTR(DE3)-RIL *Escherichia coli* (Ref. 15, kerafast) cells transformed with the His_{10}-Arg_8-ScSUMO-3C-$HsBBS9_{1-407}$ pETDuet-1 vector were grown in LB medium at 37 °C to an optical density of 0.65. Cultures were shifted to 18 °C for 30 min prior to induction with 0.2 mM isopropyl-β-D-1-thiogalactopyranoside. Expression was carried out for 16 h, after which the cultures were pelleted by centrifugation at 6,000 × *g* for 6 min. Cell pellets were resuspended in lysis buffer (50 mM potassium phosphate, pH 8.0, 500 mM NaCl, 30 mM imidazole, pH 8.0, and 3 mM β-mercaptoethanol) at 4 °C and were lysed by passage through a cell disruptor (Constant Systems) at 25 kpsi. After lysis, 1 mM PMSF and 250 units of TurboNuclease (Eton Biosciences) were added to the lysate, which was subsequently centrifuged at 9,500 × *g* for 25 min to separate soluble and insoluble fractions. Nickel-Sepharose 6 Fast Flow beads (GE Healthcare) were washed twice with lysis buffer prior to addition to the soluble fraction. Nickel binding was carried out at 4 °C for 1 h. After binding, the beads were pelleted, at 2,000 × *g*, and washed three times with lysis buffer. Six column volumes of elution buffer (250 mM imidazole, pH 8.0, 150 mM NaCl, and 3 mM β-mercaptoethanol) were used to elute the His_{10}-Arg_8-ScSUMO-3C-$HsBBS9_{1-407}$. Following elution, the protein was diluted in half with 10 mM potassium phosphate, pH 8.0, 1 mM DTT, and 0.1 mM EDTA (buffer A) and loaded onto an SP Sepharose Fast Flow cation exchange column (1 or 5 ml depending on prep size, GE healthcare). Following a 2-column volume wash with buffer A, bound protein was eluted with a 15-column volume gradient of 10 mM potassium phosphate, pH 8.0, 1 mM DTT, 0.1 mM EDTA, and 1 M NaCl (buffer B). The peak corresponding to bound His_{10}-Arg_8-ScSUMO-3C-$HsBBS9_{1-407}$ was pooled, following verification by SDS-PAGE. The N-terminal tag was cut with human rhinovirus 3C (3C) protease, added in a 1:100 ratio, and dialyzed overnight into 10 mM potassium phosphate, pH 8.0, 150 mM NaCl, 1 mM DTT, and 0.1 mM EDTA. The dialyzed sample was run over a second SP Sepharose Fast Flow column, and the flow-through fraction was collected. After the flow-through was concentrated, the sample was run over an Superdex S200 gel filtration column equilibrated in 10 mM Tris/HCl, pH 7.4, 150 mM NaCl, 1 mM DTT, and 0.1 mM EDTA (GF buffer 1). The peak corresponding to $HsBBS9_{1-407}$ was pooled and concentrated after SDS-PAGE analysis. Full-length $HsBBS9_{1-887}$ was identically expressed and purified. $HsBBS9_{405-887}$ was identically expressed and purified, with the exception that gel filtration was performed in 10 mM HEPES, pH 7.4, 150 mM NaCl, 1 mM Tris(2-carboxyethyl)phosphine, and 0.1 mM EDTA (GF buffer 2). Selenomethionine(SeMet)-derivatized $HsBBS9_{1-407}$ was expressed as described previously (16) and purified identically to native $HsBBS9_{1-407}$, with the exception that 10 mM β-mercaptoethanol was used in the nickel purification and 5 mM DTT was used in subsequent steps. The $HsBBS9_{1-407}$ point mutant purifications were performed identically to the wild type $HsBBS9_{1-407}$ nickel purification.

Limited Proteolysis—22 μl of 0.3 mg/ml $HsBBS9_{1-887}$ was digested with 2 μl of trypsin, at one of six different concentrations, in GF buffer 1. Trypsin was used at 0.1 mg/ml or diluted 1:3, 1:9, 1:27, 1:81, or 1:243 with GF buffer 1 from the 0.1 mg/ml stock. After a 30-min incubation at room temperature, the reactions were quenched with 6 μl of SDS-PAGE loading dye and boiled for 3 min. SDS-PAGE was performed on these samples, and a band of ~40 kDa was produced upon treatment with 1:243 diluted trypsin that was stable through treatment with 1:9 diluted trypsin. This band was excised, placed in 50% methanol, and subjected to LC-MS/MS.

Crystallization—Initial crystals of native $HsBBS9_{1-407}$, set up at 7.2 mg/ml, were obtained via vapor diffusion with 10% w/v PEG 4000, 0.1 M MES, pH 6.5, and 0.2 M $MgCl_2$ as part of the PEGII suite (Qiagen) in a 96-well, sitting drop tray. Single, albeit multilayered, three-dimensional crystals were observed after 2 days at 18 °C. Crystals were transferred into a cryoprotectant solution containing the crystallization condition with 20% v/v PEG 200 and cryocooled in liquid nitrogen. SeMet-derivatized $HsBBS9_{1-407}$ crystals, set up at 6.8 mg/ml, were obtained in 10% w/v PEG 4000, 0.1 M trisodium citrate, pH 6.1, and 0.15 M ammonium sulfate in 24-well, hanging drop plates at 18 °C. When compared with the native crystals, the SeMet crystals were optically superior (*i.e.* they appeared singular and unlayered) and grew larger to a final size of 0.1 mm. The SeMet crystals were transferred into a cryoprotectant solution containing the crystallization condition with 20% v/v glycerol and cryocooled in liquid nitrogen.

Structure Determination—Datasets were collected at the Advanced Photon Source user end station 24. A complete native dataset was collected to 2.4 Å, and a complete SeMet dataset, at the selenium peak wavelength, was collected to 1.8 Å. Data reduction was performed in HKL2000 (17). Molecular replacement attempts were performed in phaser-MR, part of the PHENIX suite (18). The phase problem was solved using single anomalous dispersion, and selenium positions were determined in HYSS, run as part of the PHENIX AutoSol program, for the SeMet dataset. The anomalous data extended to 2.5 Å, as assessed by phenix.xtriage. The initial model was built using PHENIX AutoBuild with the structure factors from the SeMet dataset because it was superior to the native data. Sub-

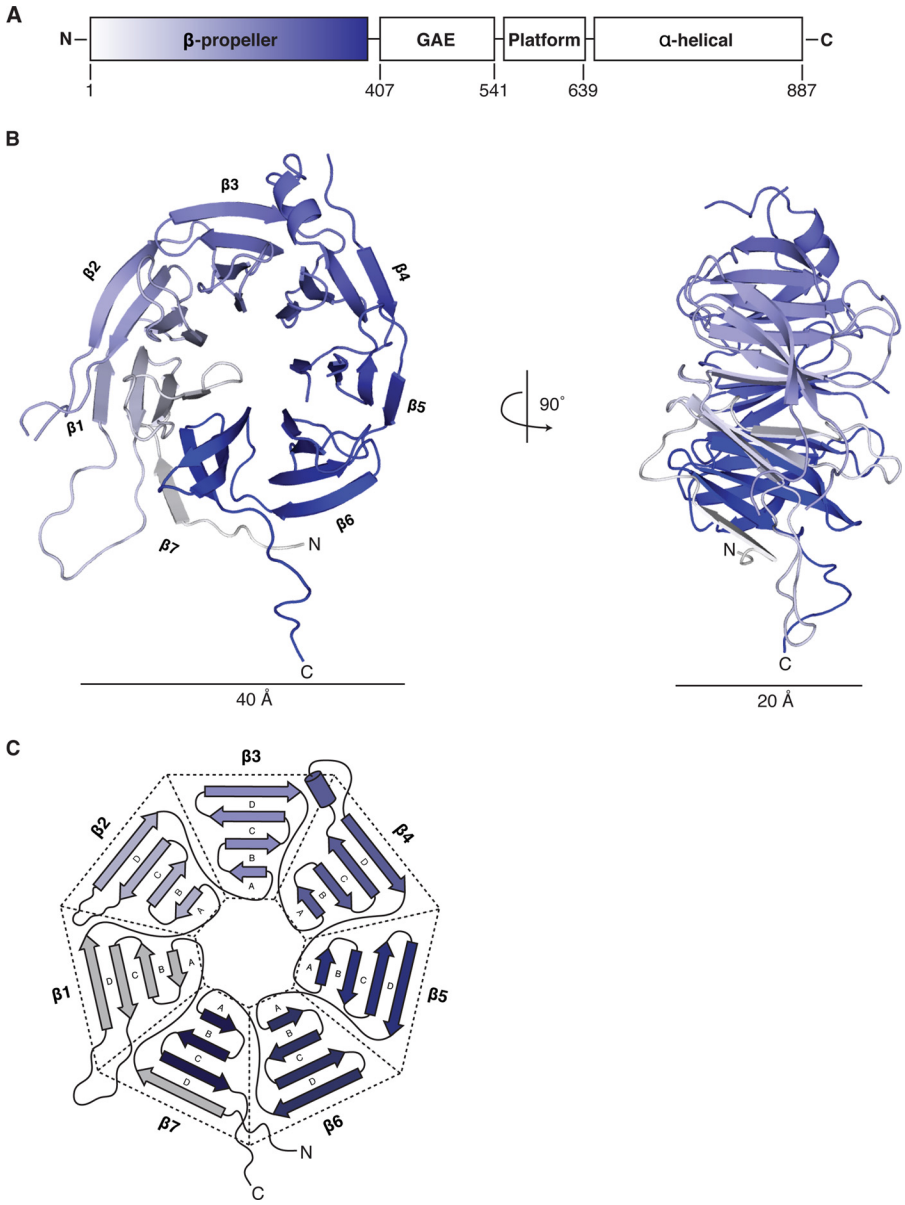

FIGURE 1. **The HsBBS9$_{1-407}$ N-terminal domain is a WD40 β-propeller.** *A*, schematic diagram of the domain architecture of HsBBS9 with the relevant domain boundaries numbered. The N-terminal β-propeller domain, solved here, is colored *white* to *blue* from N to C terminus. Following the β-propeller is a γ-adaptin ear (*GAE*) β-sandwich domain, a mixed α/β platform domain, and a C-terminal α-helical domain (10). *B*, graphic representation of the HsBBS9$_{1-407}$ β-propeller viewed from the face and, as a result of a 90° rotation, the side. The structure is colored *white* to *blue* from N to C terminus as in *A*. β-Strands are depicted as *arrows*, helices are depicted as *ribbons*, and loops are depicted as *lines*. The individual blades are labeled. *C*, detailed schematic of HsBBS9 tertiary structure, colored as in *A*.

sequent manual building was performed in Coot (19), and phenix.refine was used for refinement.

Structure Analysis—The HsBBS9$_{1-407}$ non-crystallographic symmetry (NCS) homodimer interface was analyzed using PDBePISA (20). Sequence conservation was mapped onto the surface of HsBBS9$_{1-407}$ using ConSurf (21) and a multiple sequence alignment (MSA) generated in Jalview (22) with the MUSCLE alignment algorithm. Sequences of HsBBS9$_{1-407}$ homologs were obtained via National Center for Biotechnology Information (NCBI) BLAST searches (23). The structure of HsBBS9 homologs was modeled using Phyre 2 one-to-one threading (24). Electrostatic potential was mapped onto the surface of HsBBS9$_{1-407}$ and the modeled homologs using the APBS plugin (25) in PyMOL (26). The G141R mutation was modeled into the wild type HsBBS9$_{1-407}$ structure using the mutagenesis tool in Coot.

Expression Test of HsBBS9$_{1-407}$ Constructs in Human Cell Culture—2×10^6 HEK 293T cells were grown in DMEM + 10% inactivated fetal bovine serum in 10-cm dishes. 24 h later, cells were transfected with 1 μg of DNA of either wild type HsBBS9$_{1-407}$ or HsBBS9$_{1-407}$ G141R cloned into a pRK5-FLAG expression plasmid, using PEI. 48 h after transfection, cells were harvested in Triton lysis buffer (40 mM Hepes, pH 7.4, 1% Triton X-100, 10 mM sodium pyrophosphate, 10 mM β-glycerophosphate, 2.5 mM $MgCl_2$, and one Complete protease inhibitor tablet (Roche Diagnostics)). After a 20-min incubation, the soluble and insoluble fractions were separated by a 10-min centrifugation step at 21,000 $\times$ *g*. The soluble fractions

TABLE 1
Data collection and refinement statistics

	Protein	
	$BBS9_{1-407}$ SeMet derivative[a]	$BBS9_{1-407}$ native[a]
Data collection		
Space group	$P2_12_12$	$P2_12_12$
a, *b*, *c* (Å)	136.42, 81.88, 85.65	136.14, 81.62, 85.49
α, β, γ (°)	90.0, 90.0, 90.0	90.0, 90.0, 90.0
Wavelength (Å)	0.9792	0.9792
Resolution range (Å)	44.70–1.80 (1.83–1.80)	50.00–2.40 (2.44–2.40)
Total reflections	327,946	120,972
Unique reflections	171,175	36,128
Completeness (%)	99.9 (99.9)	95.2 (78.0)
Redundancy	3.7 (3.7)	3.3 (2.7)
Anomalous completeness (%)	99.0	
R_{sym} (%)	8.6 (99.0)	14.9 (57.0)
$R_{p.i.m.}$ (%)	5.1 (59.7)	9.3 (40.1)
I/σ	23.3 (1.1)	8.8 (1.2)
$CC_{1/2}$ (%)	99.6 (58.3)	99.1 (66.9)
Refinement		
Resolution range (Å)	36.94–1.80	
R_{work} (%)	16.9	
R_{free} (%)	20.0	
Coordinate error (Å)	0.2	
Number of reflections		
Total	171,157	
R_{free} reflections	3,941	
Number of non-hydrogen atoms	6,141	
Protein atoms	5,424	
Water atoms	717	
RMS deviations		
Bond lengths (Å)	0.008	
Bond angles (°)	1.119	
Average B factors (Å^2)		
Protein	35.4	
Water	48.4	
Ramachandran (%)		
Favored (%)	97.3	
Allowed (%)	2.7	
Outlier (%)	0.0	
Clashscore	5.6	
MolProbity score	1.52	
MolProbity percentile	93rd	
PDB ID	4YD8	

[a] Organism: *H. sapiens*.

were loaded onto an SDS-PAGE gel followed by Western blotting with anti-FLAG (Cell Signaling Technologies) and anti-Raptor (for loading control) antibodies.

Analytic 3C Proteolysis of His_{10}-Arg_8-ScSUMO-3C-$HsBBS9_{1-407}$ Point Mutants—2 μl of 1 mg/ml 3C protease was added to 48 μl of nickel eluate, and the reaction was allowed to proceed for 30 min at 37 °C. The reaction was quenched by the addition of 5× SDS-loading dye followed by boiling for 5 min. 10 μl of boiled sample was loaded onto an SDS-PAGE gel for analysis.

Size Exclusion Chromatography (SEC) Experiments—The $HsBBS9_{1-407}$ concentration-dependent shift experiment was performed in GF buffer 2. 100 μl of $HsBBS9_{1-407}$ was loaded onto a Superdex S75 10/300 size exclusion column at 10, 5, 2.5, or 1 mg/ml. The runs were performed in direct succession, and dilutions were performed immediately prior to the size exclusion run. $HsBBS9_{405-887}$ concentration-dependent shift experiment was identically performed, except a Superdex S200 10/300 column was used. The initial $HsBBS9_{1-407}$, $HsBBS9_{405-887}$ binding test was performed in GF buffer 1. $HsBBS9_{1-407}$ and $HsBBS9_{405-887}$ were mixed in an equimolar ratio and, after incubation at 4 °C, were loaded onto a Superdex S200 10/300 column equilibrated in GF buffer 1. For the low salt binding test, $HsBBS9_{1-407}$ and $HsBBS9_{405-887}$ were mixed in an equimolar ratio in 10 mM Tris/HCl, pH 7.4, 100 mM NaCl, 10% glycerol, 1 mM DTT, and 0.1 mM EDTA prior to loading onto an S200 10/300 column equilibrated in the same buffer. For the high-salt binding test, equimolar amounts of $HsBBS9_{1-407}$ and $HsBBS9_{405-887}$ were mixed in 10 mM Tris/HCl, pH 7.4, 500 mM NaCl, 1 mM DTT, and 0.1 mM EDTA prior to loading onto an appropriately equilibrated Superdex S200 10/300 column. The data were plotted in Prism (GraphPad Software).

Equilibrium Analytical Ultracentrifugation—Equilibrium analytical ultracentrifugation (AUC) on $HsBBS9_{1-407}$ and $HsBBS9_{405-887}$ was performed, in GF buffer 2, in an Optima XL-1 analytical ultracentrifuge (Beckman Coulter) using an AN-50 titanium rotor (Beckman Coulter) with a six-channel, Epon rectangular centerpiece (1.2 cm, Beckman Coulter). $A_{280\,nm}$ measurements were taken once the samples reached equilibrium, and buffer contribution to the absorbance was removed using a reference cell, which contained GF buffer 2. $HsBBS9_{1-407}$, at 0.37 mg/ml, was spun to 9,500, 12,000, and 18,000 rpm. Five absorbance scans were performed at each speed, with three replicates per scan. $HsBBS9_{405-887}$ at 1.2 mg/ml, in duplicate, was spun to 9,500, 14,000, and 17,000 rpm. Three absorbance scans were performed at each speed, with three replicates per scan. The equilibrium absorbance data were analyzed using UltraScan II (27) and fit using nonlinear least squares fitting.

Results

Structure of the $HsBBS9_{1-407}$ N-terminal Domain—To structurally characterize *H. sapiens* BBS9, we recombinantly expressed the protein in *E. coli*. Full-length $HsBBS9_{1-887}$ suffered from low yield. To identify a construct suitable for crystallization, we performed a limited tryptic digest and identified a protease-resistant HsBBS9 fragment corresponding to the N-terminal domain, residues 1–374, via LC-MS/MS (Fig. 1*A*, data not shown). Subsequent expression, in bacteria, of $HsBBS9_{1-407}$ yielded sufficient material for structural analysis. We obtained crystals of the HsBBS9 N-terminal domain, which diffracted to 2.4 Å (Table 1). Despite knowing that $HsBBS9_{1-407}$ likely adopts a β-propeller fold, we found no molecular replacement solutions using various β-propeller templates. We also employed the Wide-Search Molecular Replacement (WSMR) protocol, available through the SBgrid software consortium (28), without success. The structure was ultimately solved using experimental phases that were obtained through single anomalous dispersion on SeMet-derivatized $HsBBS9_{1-407}$ crystals, which diffracted to 1.8 Å (Table 1). The model was refined against the SeMet dataset to a final R_{work} of 16.9% and an R_{free} of 20.0%. Overall the structure is well ordered, with an average protein B-factor of 35.4 Å^2. Exceptions to this include the protein termini, as residues 1–2 and 370–407 are disordered, as well as several loop regions, where residues 113–117, 219–232, and 254–255 could not be built with confidence.

$HsBBS9_{1-407}$ comprises seven anti-parallel, four-stranded β-sheets that are radially arranged around a central, solvent-accessible pore (Fig. 1, *B* and *C*). $HsBBS9_{1-407}$ is ~40 Å in diameter across its face and 20 Å in height when viewed side-on.

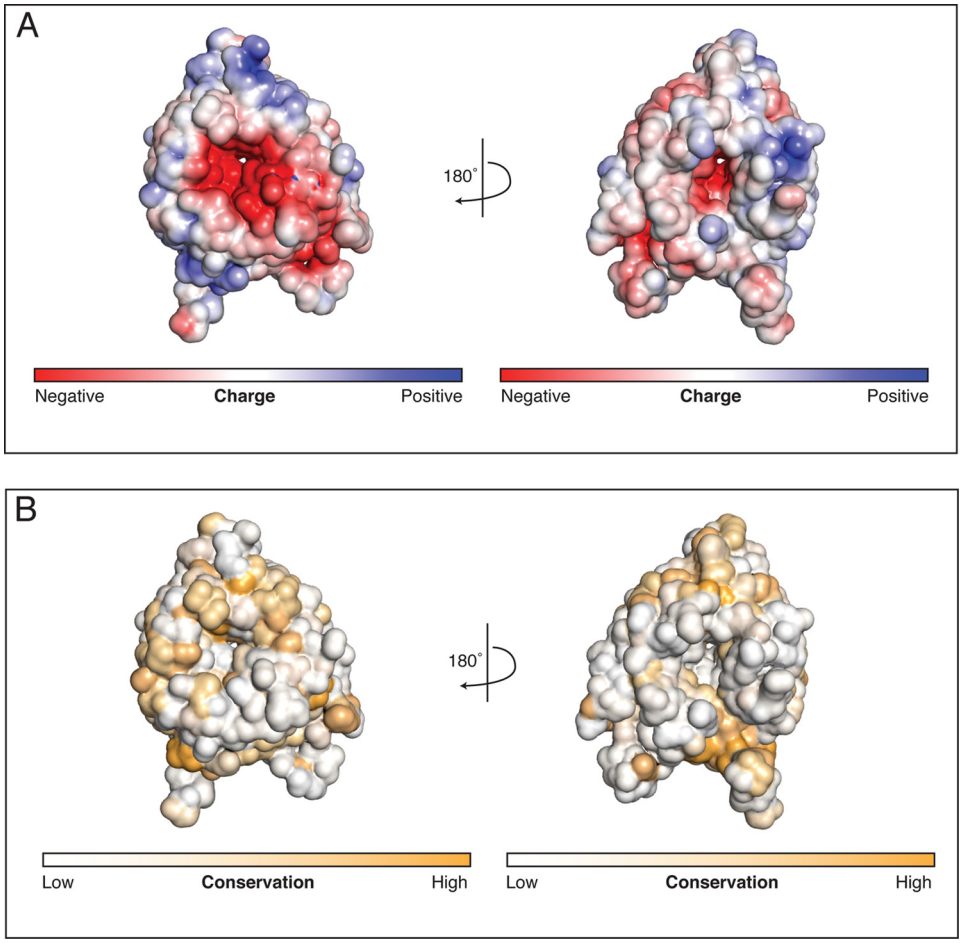

FIGURE 2. **A negative patch exists around the pore on one face of the HsBBS9$_{1-407}$ β-propeller.** *A*, electrostatic potential mapped onto the solvent-accessible surface of HsBBS9$_{1-407}$. The electrostatic potential is colored from −5 *kT/e* (negative, *red*) to +5 *kT/e* (positive, *blue*). Both faces, rotated by 180° with respect to each other, are shown. *B*, sequence conservation mapped onto the solvent-accessible surface of HsBBS9$_{1-407}$. Conservation is colored from *white* (not conserved) to *orange* (conserved), and views are as in *A*.

HsBBS9$_{1-407}$ is a closed, seven-bladed β-propeller of the WD40 repeat family, which canonically is characterized by motifs 40 amino acids in length that end in tryptophan-aspartate motifs (29). Blades one through six (β1–β6), numbered from the N to the C terminus, each begin with the innermost strand ("A") and trace to the outermost strand ("D"), which then connects to the A strand of the next blade. β7 is an exception to this topology because the N-terminal β-strand of the protein serves as the outermost D strand of this C-terminal, three-stranded β-sheet (A–C). This irregular connectivity, termed a "Velcro" closure, is common among β-propellers (30, 31). By physically tethering the N- and C-terminal blades together, this Velcro closure likely stabilizes the HsBBS9$_{1-407}$ fold by preventing opening of the propeller. HsBBS9$_{1-407}$ contains additional elaborations between the C and D strands of various blades, such as the helical insertion of β4 and the extended loops of β1 and β2.

Structural Analysis of the HsBBS9$_{1-407}$ β-Propeller—With the HsBBS9$_{1-407}$ structure in hand, we sought to gain insight into the function of the β-propeller through analogy to structurally similar proteins. We performed structure-based homology searches using the DALI server (32). In total, over 100 significant homologs were found (data not shown), as determined by *Z* scores above a predetermined threshold ($Z > 10$), and greater than half of the hits had an RMSD below 3.0 Å. The large number of hits obtained likely is due to the fact that HsBBS9$_{1-407}$ contains fairly few structural elaborations beyond the conserved, core scaffold that defines a propeller fold. Such elaborations would undoubtedly discriminate in the DALI search between various subclasses of seven-bladed propellers, reducing the number of significant solutions obtained. Despite this, three structural homologs, through their *Z* scores, stood out above the rest. The top scoring homolog was the recently solved *C. reinhardtii* (Cr) BBS1 N-terminal β-propeller (Protein Data Bank (PDB): 4v0m_B, RMSD 2.8 Å over 296 amino acids, SeqID 12%, $Z = 31.5$), which functions by binding the Arl6-GTPase that tethers the BBSome complex to membranes (12). The CrBBS1 N-terminal domain is also a fairly minimal propeller with few structured insertions. As the top solution, the CrBBS1 N-terminal domain and HsBBS9$_{1-407}$ are more similar to each other than they are to other propellers. This result likely extends to the other predicted, seven-bladed propellers within the BBSome, namely the BBS2 and BBS7 N-terminal domains. The other two high-scoring homologs were the WD40 domain of a *Saccharomyces cerevisiae* serine/threonine-protein kinase (Vps15, PDB: 3GRE_A, RMSD 2.4 Å over 291 amino acids, SeqID 11%, $Z = 28.6$), which binds the protein Gpa1 (33), and a WD40 protein of the Ski complex (Ski8, PDB: 1SQ9_A, RMSD 2.8 Å over 292 amino acids, SeqID 10%, $Z =$

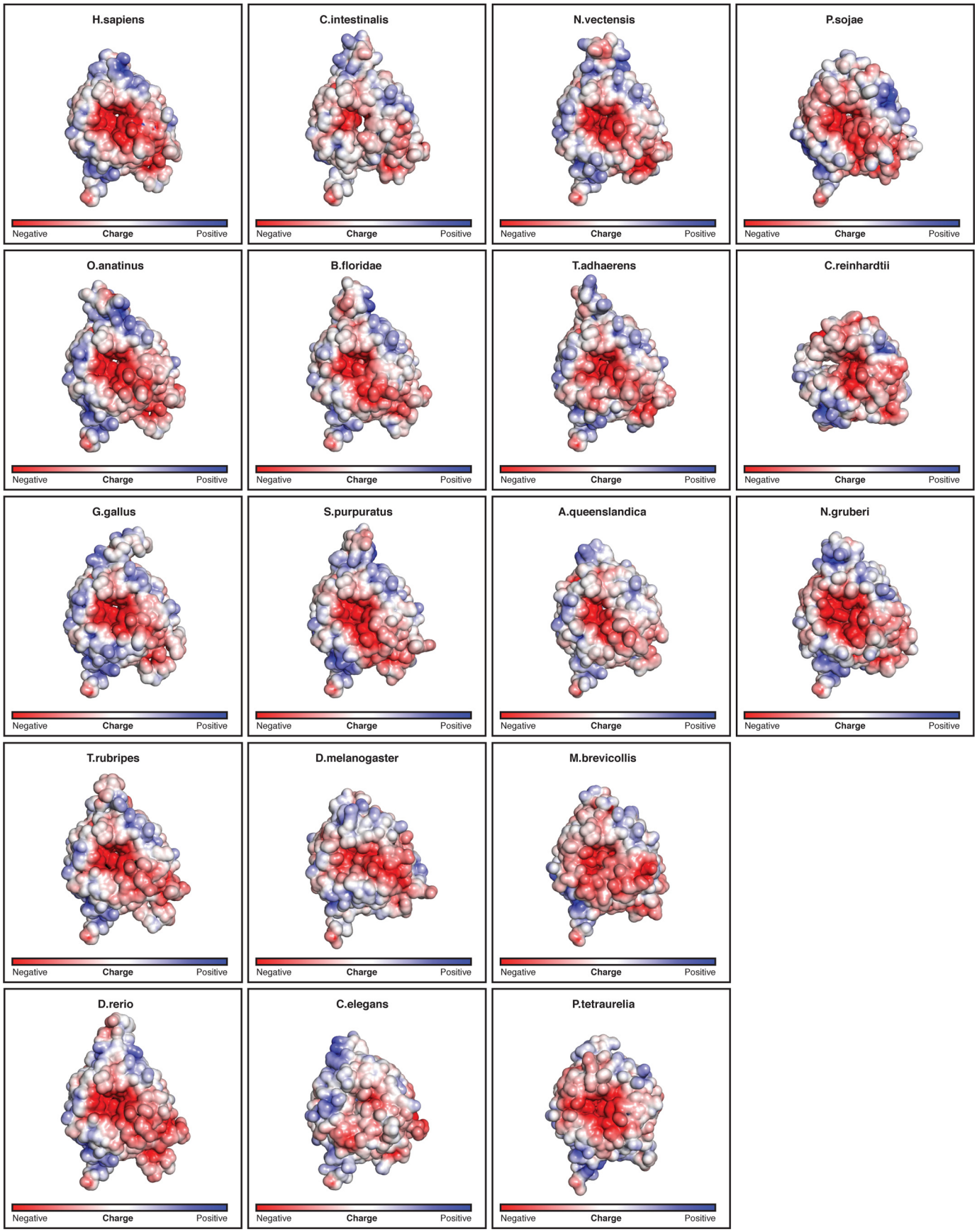

FIGURE 3. **Electrostatic potential mapped onto the solvent-accessible surface of HsBBS9$_{1-407}$ and the modeled structures of the 17 homologs from the MSA, depicted in Fig. 8.** Views and coloring are identical to Fig. 2*A* (*left*), with the electrostatic potential calculated from −5 *kT/e* to +5 *kT/e*.

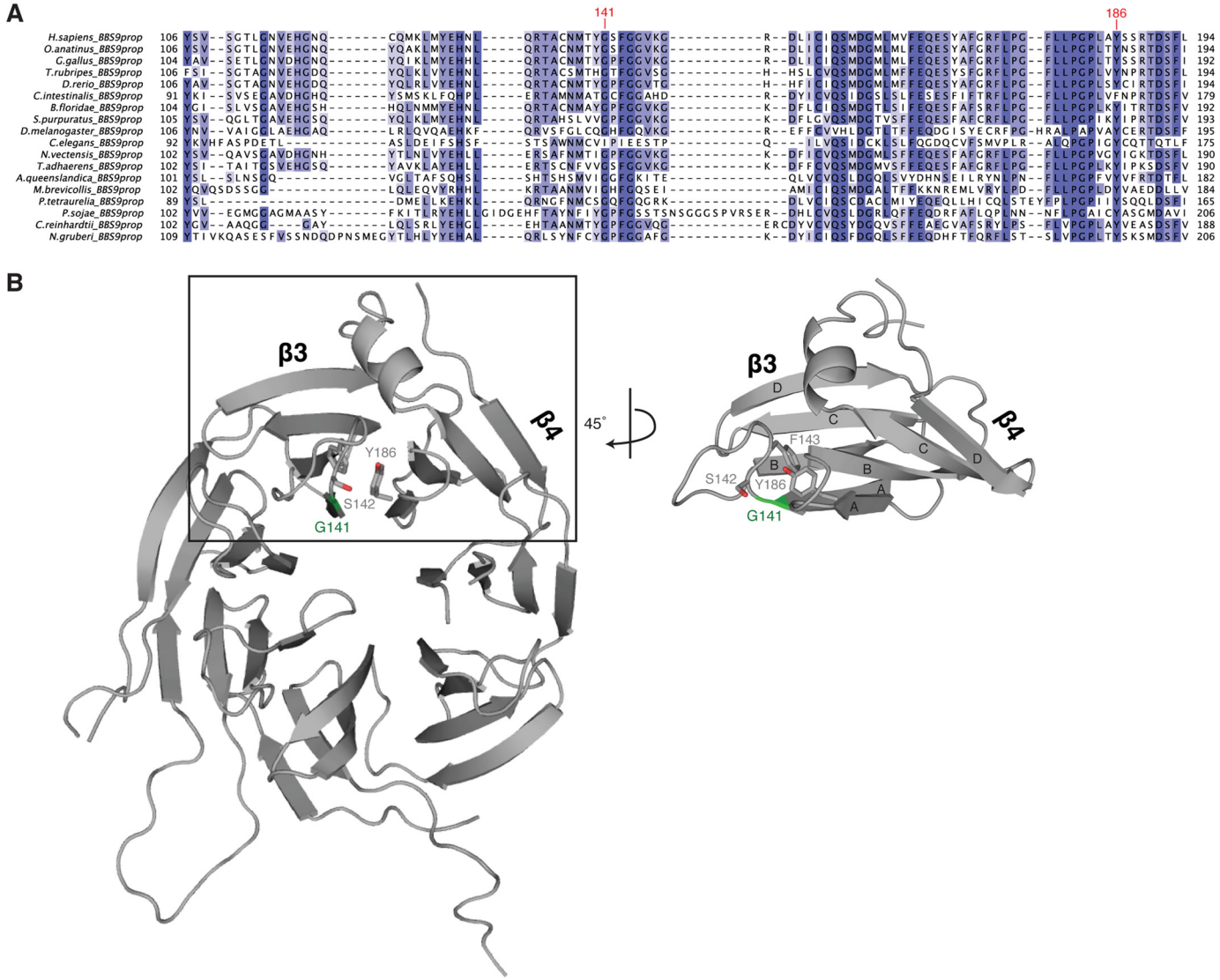

FIGURE 4. **Location of Gly^{141} in HsBBS9$_{1-407}$.** *A*, fragmentary MSA of BBS9$_{1-407}$ depicting the position and conservation of Gly^{141}, labeled in *red*. Positions are colored *white* to *blue*, according to increasing sequence identity. *B*, graphic representation of HsBBS9$_{1-407}$ (*gray*) showing the position of Gly^{141} (*green*) and surrounding residues of interest as sticks. The *boxed region* is rotated by 45° for clarity.

27.4), which binds the proteins Ski2 and Ski3 (34). These hits illustrate that β-propellers are among the most common folds in biology, found in a wide range of proteins with diverse functions. Many β-propellers function as platforms for protein-protein interactions (31).

Given the propensity of β-propellers to form protein-protein interactions, we mapped the electrostatic potential onto the surface of HsBBS9$_{1-407}$ to see whether a charged binding site is apparent. This analysis reveals a large negative patch around the central pore on one face of the propeller (Fig. 2*A*). To determine whether this feature is conserved, we created an MSA sampling a diverse set of 17 BBS9 homologs and mapped sequence conservation onto the surface of HsBBS9$_{1-407}$ (Fig. 2*B*). This analysis revealed that the conservation of the charged residues responsible for the negative potential and those lining the pore opening, in general, is poor. Before dismissing this patch as an oddity of *H. sapiens*, we decided to create structural models of the 17 BBS9 β-propellers in the MSA, based on the *H. sapiens* structure, and map their surface electrostatic potential. This negative patch is notably present in BBS9 β-propellers across the MSA (Fig. 3). Although individual sequence positions are not conserved, these homologs have negatively charged residues at different positions and a relative lack of positive charge in the vicinity of the pore. Solvent-exposed carbonyl oxygens additionally contribute to the negative potential of this surface.

Structural Analysis of HsBBS9 G141R, Which Causes BBS—Homozygosity mapping in a small, consanguineous family has revealed a SNP within the BBS9 N-terminal domain that causes BBS in humans (13). This SNP confers a missense mutation on residue 141, mutating the glycine at that position to an arginine. Gly^{141} is strictly conserved across the MSA with the exception of *C. elegans* BBS9, which has an Ile at this position and generally poor conservation in the region surrounding this residue (Fig. 4*A*). With the HsBBS9$_{1-407}$ crystal structure at hand, we can model the G141R mutation into the structure to assess why it is pathological. Gly^{141} is positioned within the tightly packed C terminus of the A strand of blade β3 (Fig. 4*B*), on the opposite

face of the negatively charged patch described in Fig. 2. Immediately downstream of Gly[141] is a highly curved loop that traces perpendicular to the A strand, packing Phe[143] into the hydrophobic core of blade β3, before changing direction by 180° (Fig. 5*A*). Analyzing the Ramachandran plot reveals that Gly[141] occupies a special position with dihedral angles that, although

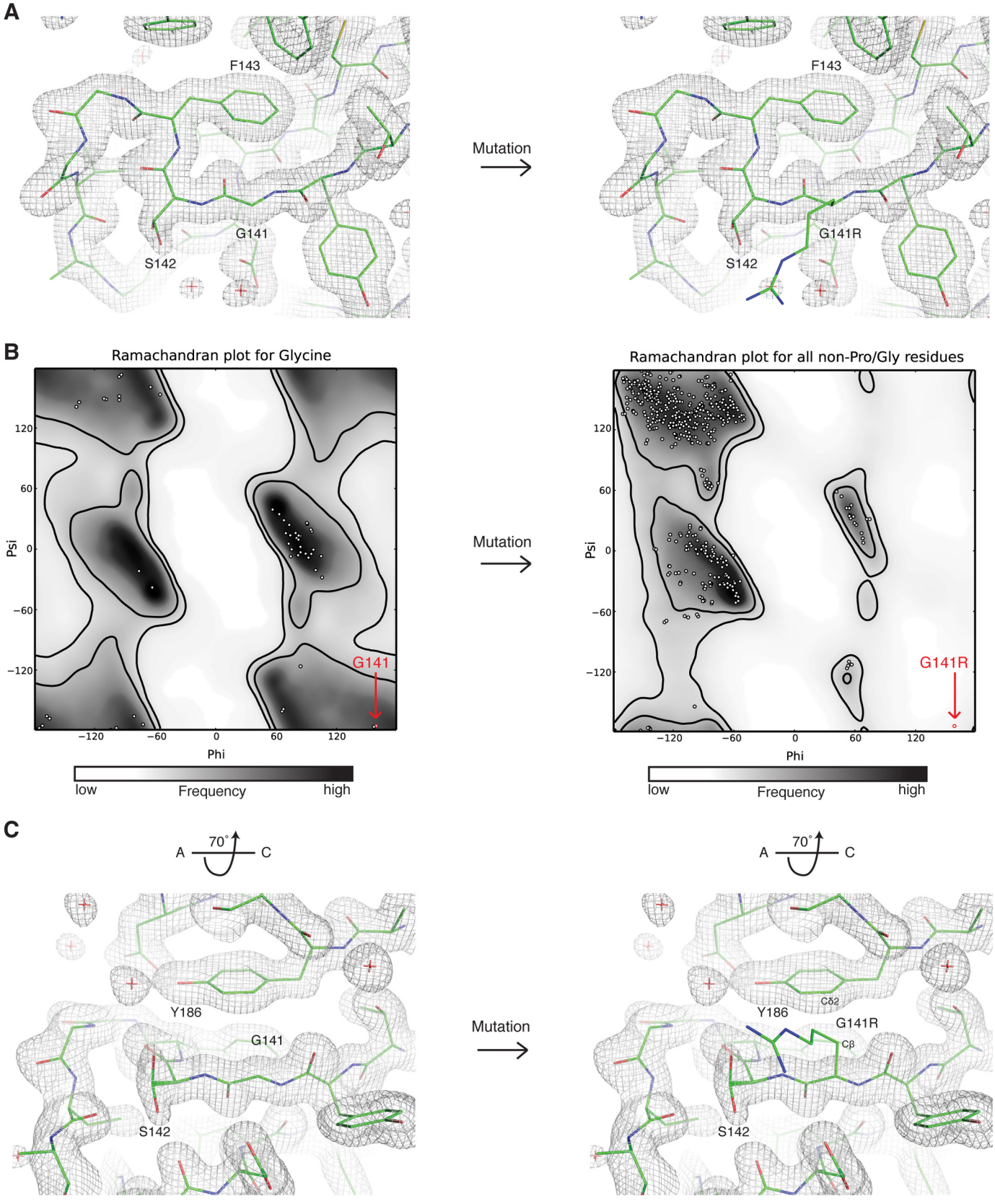

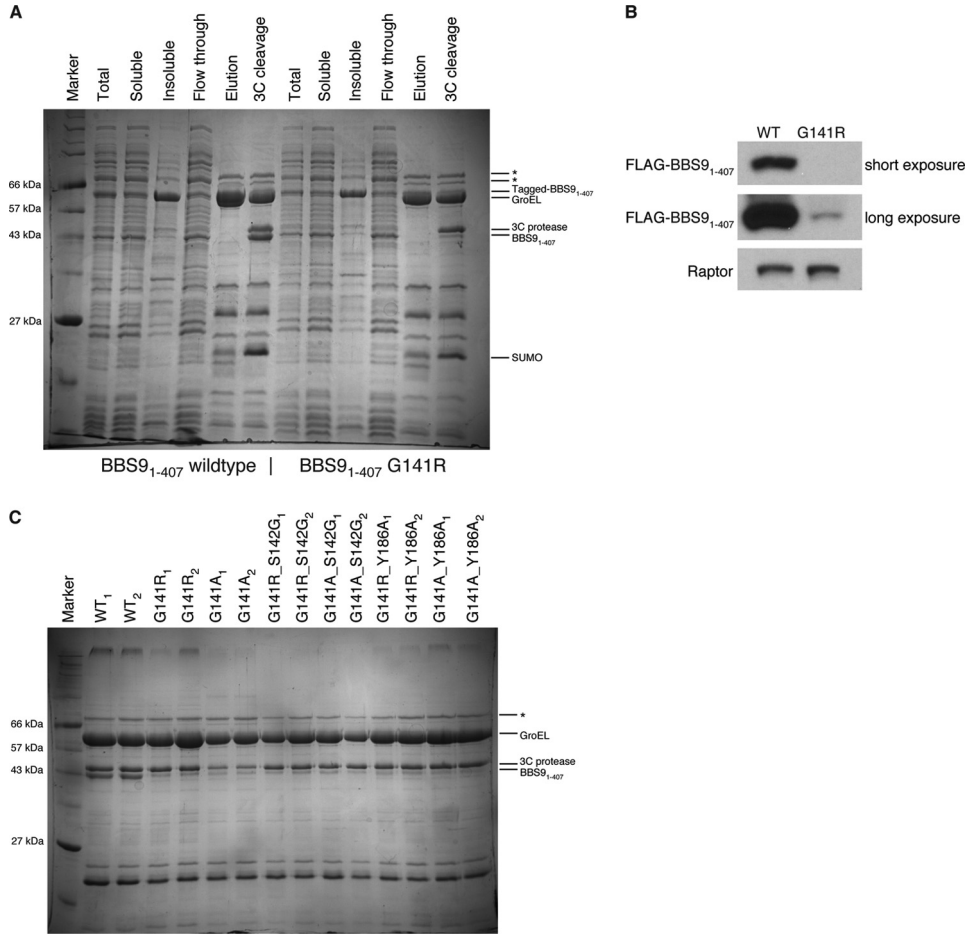

FIGURE 6. **Soluble protein levels of HsBBS9$_{1-407}$ G141R are substantially reduced when compared with wild type.** *A*, Coomassie Brilliant Blue-stained SDS-PAGE gel of nickel affinity pulldown experiment, comparing purified protein levels of WT HsBBS9$_{1-407}$ (*left*) and HsBBS9$_{1-407}$ G141R (*right*) expressed in *E. coli*. Lane labels refer to samples taken throughout the nickel affinity purification: *Total*, crude lysate; *Soluble*, supernatant after lysate clarification; *Insoluble*, pellet after lysate clarification; *Flow through*, soluble sample that did not bind to nickel; *Elution*, soluble sample that bound nickel and was eluted with imidazole; *3C cleavage*, eluate treated with 3C protease for 30 min at 37 °C for tag removal. In the elution fractions, the largest two bands (labeled with *) are *E. coli* contaminants. Other bands are labeled accordingly. *B*, anti-FLAG Western blot of soluble fraction from expression test of FLAG-tagged, wild type HsBBS9$_{1-407}$ (*left*) and FLAG-tagged HsBBS9$_{1-407}$ G141R (*right*) in HEK 293T cells. Two exposure times are shown, for clarity. Anti-Raptor antibody is used for the Raptor loading control. *C*, Coomassie Blue-stained SDS-PAGE gel from nickel affinity pulldown of HsBBS9$_{1-407}$ point mutants in *E. coli*. Shown are the 3C-treated, nickel elution fractions for two different clones of WT, disease mutant (G141R), and designed point mutants (labeled accordingly, above gel).

accessible to glycine, are forbidden to all other amino acids due to steric restraints imposed by the invariant presence of a β-carbon atom (Fig. 5*B*). Additionally, modeling all possible rotamers of arginine in position 141 of HsBBS9$_{1-407}$ reveals a steric clash between the β-carbon of the arginine side chain and the Cδ2 carbon of the Tyr^{186} aromatic ring (Fig. 5*C*). These carbon atoms are only 2.4 Å apart, which results in an overlap of 1 Å when hydrogen atoms are included. Based on these backbone and side chain restraints, we posit that there is an absolute structural requirement for a glycine at position 141.

To test the effect of the G141R mutation in solution, we expressed the His$_{10}$-Arg$_8$-ScSUMO-3C-tagged HsBBS9$_{1-407}$ G141R point mutant in *E. coli* and compared the amount of purified protein with the level of wild type His$_{10}$-Arg$_8$-ScSUMO-3C-tagged HsBBS9$_{1-407}$ using a nickel affinity pulldown assay. When compared with wild type, the yield of HsBBS9$_{1-407}$ G141R after nickel affinity purification is marginal (Fig. 6*A*). This result is clearer after removal of the His$_{10}$-Arg$_8$-ScSUMO tag with 3C protease. Tagged HsBBS9$_{1-407}$ runs just under the 66-kDa marker in the same position as the *E. coli* GroEL chaperone, as determined by LC-MS/MS (data not shown), whereas untagged HsBBS9$_{1-407}$ runs unobstructed beneath the 3C protease band near the 43-kDa marker. This difference in protein level is reproducibly seen and is not due to clonal variation as the same result was obtained using five different clones of HsBBS9$_{1-407}$ G141R-

FIGURE 5. **Detailed view of the position of glycine 141, which reveals steric restraints on the identity of this residue.** *A*, view of main chain topology up- and downstream of glycine 141. The protein chain (*green sticks*) is shown for glycine 141 (*left*) or the G141R mutation (*right*) modeled as the most sterically permissive rotamer (fewest clashes). The final $2F_o - F_c$ electron density map is represented as a *gray mesh*. *B*, Ramachandran plots for glycine (*left*) or non-proline/glycine residues such as arginine (*right*). *White dots* show the distribution of ϕ and ψ angles for residues in the HsBBS9$_{1-407}$ structure. The position of glycine 141 and the G141R point mutant is shown (*red dot*). Favored regions (*inner black line*) and allowed regions (*outer black line*) are shown, and the plot is colored from *white* to *black* according to frequency of occurrence in the Top500 database of high-resolution protein structures. These plots were generated in PHENIX (18). *C*, view of the G141R-Tyr186 steric clash, rotated by 70° around the *x* axis relative to *A*. The arginine side chain is pointing out of the page. The atoms in close contact are labeled.

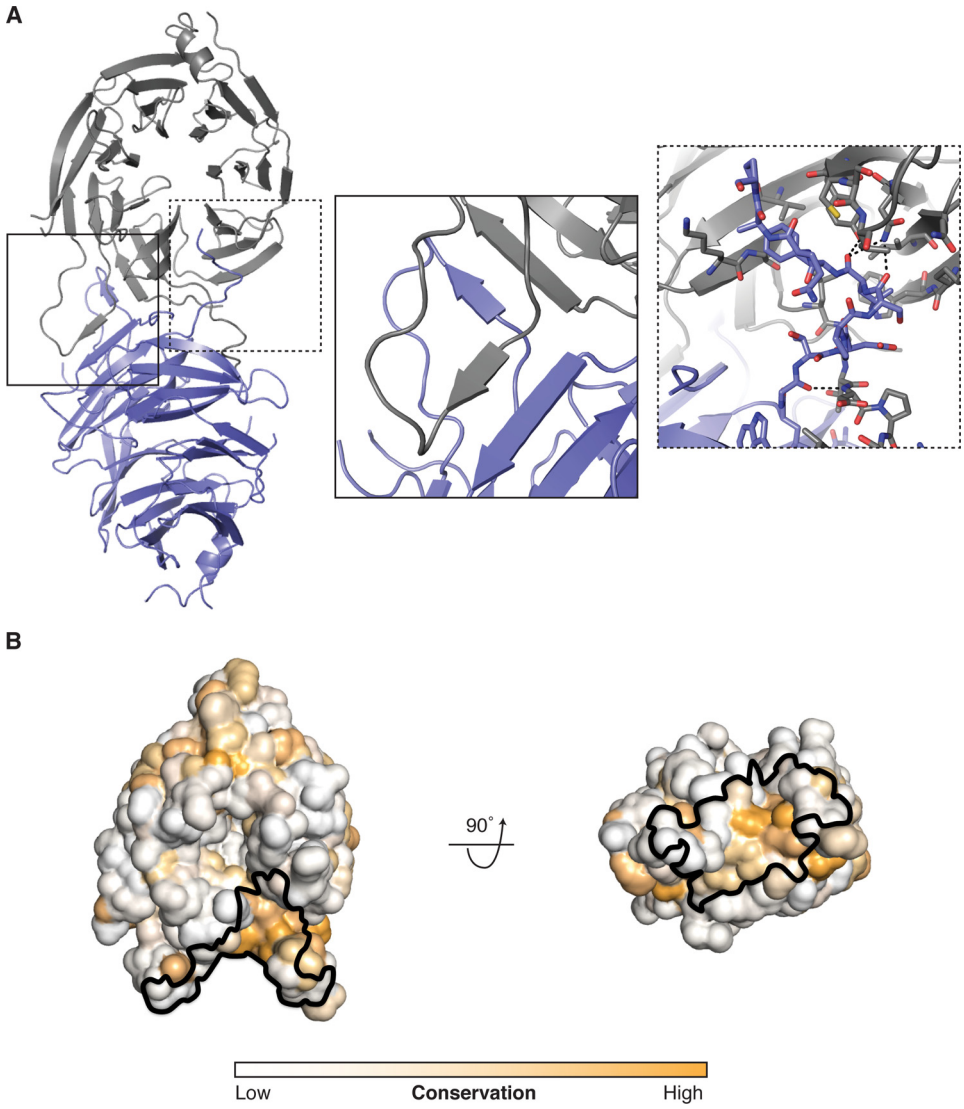

FIGURE 7. **The HsBBS9$_{1-407}$ β-propeller forms a homodimer in the crystal lattice.** *A*, overview of the HsBBS9$_{1-407}$ homodimer. Each NCS copy (one shown in *blue*, the other shown in *gray*) is depicted as a graphic representation. *Inset left (solid line)*, close-up view of the β-strand domain swap. *Inset right (dotted line)*, close-up view of the C-terminal loop domain swap, with interacting residues shown as sticks. *Black dotted lines* depict hydrogen bonds. The *inset* views are rotated relative to the overview for clarity. *B*, conservation mapped, from low (*white*) to high (*orange*), onto a solvent-accessible surface representation of HsBBS9$_{1-407}$ in the same orientation as the *gray copy* in *A*. The binding site of the symmetry mate is outlined (*black*). A 90° rotation of this starting orientation is shown, for clarity.

producing *E. coli* (data not shown). To confirm that the observed difference is not an artifact of bacterial expression, we transiently transfected FLAG-tagged HsBBS9$_{1-407}$ and HsBBS9$_{1-407}$ G141R into the HEK 293T human cell line. Anti-FLAG Western blotting of the soluble fraction reveals that HsBBS9$_{1-407}$ G141R is barely visible, whereas the wild type protein is detected easily (Fig. 6*B*).

A prediction of our hypothesis, that a glycine is essential at position 141, is that any mutation regardless of identity will be equally deleterious. To test this prediction, we created a series of point mutants and tested their protein levels in *E. coli* again by analyzing the amount of protein isolated in a nickel pull-down on SDS-PAGE, after 3C cleavage of the affinity tag (Fig. 6*C*). Consistent with this prediction, mutating Gly^{141} to alanine results in the same virtual absence of the protein as observed with the G141R mutant. Interestingly, mutating the neighboring residue, Ser^{142}, to a glycine fails to rescue protein levels in the context of both the arginine and the alanine mutant at position 141. Additionally, an attempt to remove the predicted side chain steric clash of Arg^{141} with Tyr^{186} by mutating the latter to alanine (Y186A) also failed to rescue purifiable protein amounts. In summary, the mutational analysis and the expression tests in two different hosts strongly suggest that the G141R mutation promotes a folding defect, effectively rendering HsBBS9 non-functional.

The HsBBS9$_{1-407}$ β-Propeller Forms a Homodimer in the Crystal Lattice—We analyzed packing contacts within our crystal to see whether potentially biologically relevant interactions are recapitulated within the lattice. The metric for relevance here is the predicted size or strength of a particular interaction. One such large contact occurs between two NCS mates where the β-propellers bind in a side-on fashion (Fig. 7*A*). The interface is symmetrical and primarily characterized by two domain swaps. In the first, each NCS mate contributes a fifth β-strand

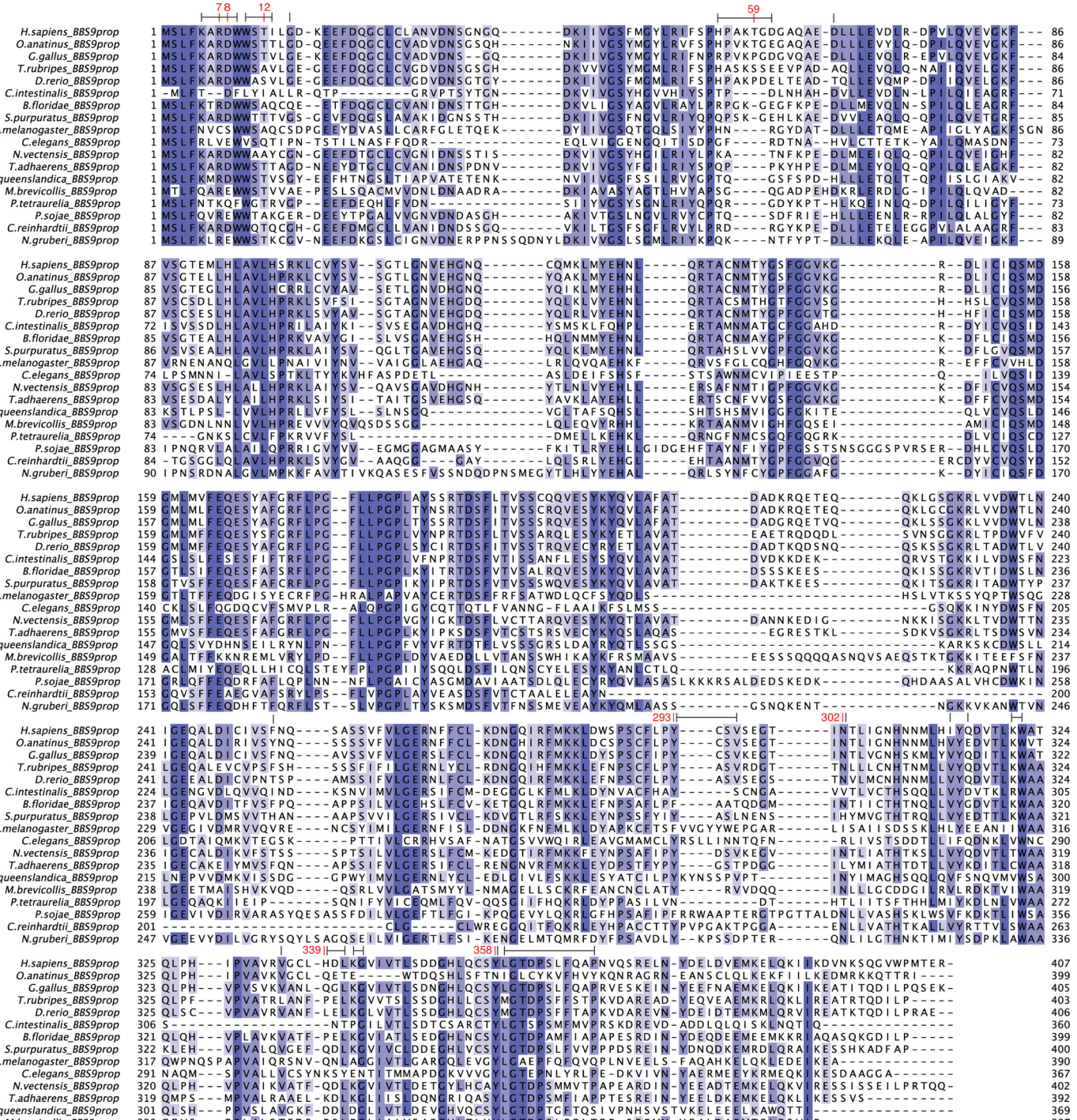

FIGURE 8. **MSA of the BBS9 N-terminal domain from 18 BBS9-containing eukaryotes.** Residues are colored according to sequence identity, from *white* to *blue*. Numbered above the MSA, in *red*, are residues that participate in sequence-specific interactions within the HsBBS9 homodimer interface (hydrogen bonds and salt bridges). Residue ranges marked by *black lines* above the MSA denote amino acids buried by the interface (van der Waals interactions). Species were chosen for inclusion in the MSA based on Bork and co-workers and Dawson and co-workers (44, 45), to obtain a diverse sampling of eukaryotes and are ordered according to increasing distance from *Homo sapiens*. BBS9 is notably absent from land plants and fungi. The alignment comprises 13 metazoa (7 Chordata, 1 Arthropoda, 1 Nematoda, 1 Echinodermata, 1 Placozoa, 1 Cnidaria, and 1 Porifera), 1 Excavata, 1 protist (choanoflagellate), 1 plantae (green algae/Chlorophyta), and 2 protozoa (Chromalveolata).

to blade β7 of the other HsBBS9 copy, forming a parallel β-sheet. This contributed strand emanates from the loop region between the C and D strands of blade β1 (Fig. 7*A*; *inset*). In the second domain swap, the C-terminal loop inserts into a surface pocket, between blades β6 and β7, on each NCS mate. In addition, the N-terminal loop packs against the loop-connecting strands A and B of blade β7. In total, this dimeric interface buries a surface area of 1,731 Å^2 and comprises 24 hydro-

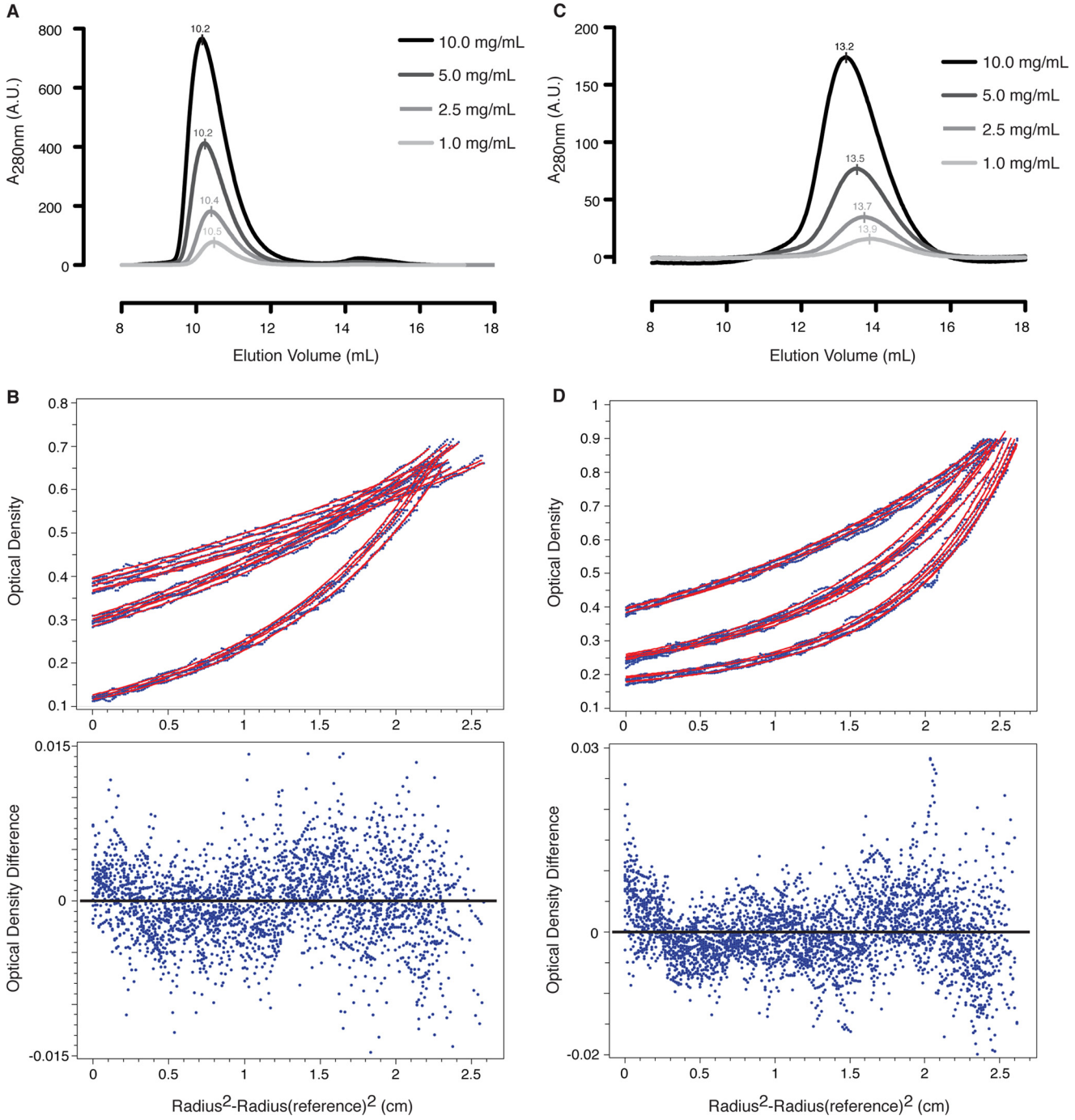

FIGURE 9. **The HsBBS9$_{1-407}$ β-propeller does not form a homodimer in solution, unlike the HsBBS9$_{405-887}$ C-terminal half.** *A*, overlaid absorbance traces from SEC experiment on HsBBS9$_{1-407}$ at 1 mg/ml (*light gray*), 2.5 mg/ml (*gray*), 5 mg/ml (*dark gray*), and 10 mg/ml (*black*). Elution volume is indicated above each peak. *A.U.*, absorbance units. *B*, *top*, absorbance data, at 280 nm, for HsBBS9$_{1-407}$ from equilibrium AUC experiment plotted against cell radius position in centimeters (see "Experimental Procedures" for details). Individual absorbance measures are depicted as *blue dots*, and non-linear least squares fits are shown (*red lines*). Data and fits are plotted for HsBBS9$_{1-407}$ at 9,500 rpm (*top*), 12,000 rpm (*middle*), and 18,000 rpm (*bottom*). *B*, *bottom*, residuals for model fit to data. The zero position is indicated by a *black line*. *C*, overlaid absorbance traces from SEC experiment on HsBBS9$_{405-887}$ at 1 mg/ml (*light gray*), 2.5 mg/ml (*gray*), 5 mg/ml (*dark gray*), and 10 mg/ml (*black*). *D*, absorbance data, at 280 nm, for HsBBS9$_{405-887}$ from equilibrium AUC experiment plotted as in *B*. Data and fits are plotted for HsBBS9$_{405-887}$ at 9,500 rpm (*top*), 14,000 rpm (*middle*), and 17,000 rpm (*bottom*).

gen bonds and two salt bridges for a predicted free energy change of −23.8 kcal/mol upon binding (20).

To validate this interaction, we examined sequence conservation on the HsBBS9$_{1-407}$ structure. This analysis reveals that the interface of the NCS dimer is moderately conserved, which makes it difficult to rule out this interaction as a crystallization artifact (Fig. 7*B*). By examining the MSA in detail, it becomes clear that two interface features are poorly conserved (Fig. 8). The first is the Asp^8–His^{339} salt bridge, which can only be formed in a subset of species. Second, the β-strand domain swap is not conserved. The loop that contributes the fifth β-strand to blade β7 (residues 53–68 in *H. sapiens*) is of variable length in the MSA. Specifically, 11 out of 18 species in the alignment have a 4- or 5-amino acid deletion in this loop, likely

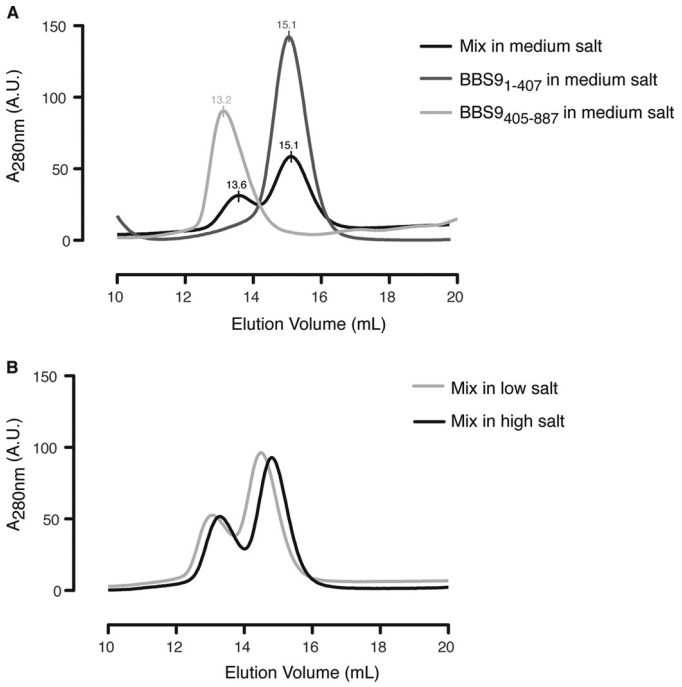

FIGURE 10. **HsBBS9$_{1-407}$ and HsBBS9$_{405-887}$ do not bind to each other on SEC.** *A*, absorbance trace overlay from SEC on HsBBS9$_{1-407}$ (*dark gray*), HsBBS9$_{405-887}$ (*light gray*), and the two mixed together in a 1:1 ratio (*black*) in medium salt buffer (150 mM NaCl; see "Experimental Procedures" for complete buffer composition). Peak elution volumes are noted above the curves and are approximately the same after mixing, indicating a lack of complex formation. *A. U.*, arbitrary units. *B*, absorbance trace overlay from SEC on HsBBS$_{1-407}$ and HsBBS$_{405-887}$ mixed in low salt buffer (100 mM NaCl and 10% v/v glycerol, *light gray*) and high-salt buffer (500 mM NaCl, *black*). A net shift of both peaks occurs as a result of buffer differences. A third peak of smaller elution volume does not form, indicating that the proteins do not bind to each other.

making it too short to contribute this strand to the neighboring BBS9 β-propeller. Removing this interaction, however, still leaves the majority of Van der Waals contacts and 14 hydrogen bonds within the homodimer interface intact.

Biophysical Characterization of HsBBS9 in Solution—To determine whether HsBBS9$_{1-407}$ dimerizes in solution, we performed SEC with purified HsBBS9$_{1-407}$, yielding a single peak at the approximate size of a monomer. Increasing the concentration of HsBBS9$_{1-407}$ had no effect on the elution volume, inconsistent with dimer formation (Fig. 9*A*). Due to the limited resolution of SEC, we set out to validate this result with equilibrium AUC. We tested a single protein concentration at three different speeds. The data for all three speeds fit globally to an ideal, non-interacting, one-component system with a molecular mass of 44,910 Da, indicative of a monomeric species (calculated molecular mass = 45,862 Da (35)) (Fig. 9*B*). These results demonstrate that the HsBBS9$_{1-407}$ homodimer does not form in solution.

To determine whether other regions of HsBBS9 oligomerize, we performed SEC on the C-terminal half of the protein, HsBBS9$_{405-887}$, which contains three folded domains according to structure prediction and can be recombinantly expressed and purified from *E. coli*. Unlike HsBBS9$_{1-407}$, the elution volume of HsBBS9$_{405-887}$ decreases upon increasing protein concentration (Fig. 9*C*). The observed decrease in elution volume and broadening of the peak is consistent with dimer formation. To verify this result, we performed equilibrium AUC on HsBBS9$_{405-887}$ at a single concentration, in duplicate, spun at three different speeds. The data fit well to a monomer-dimer equilibrium model, with a fitted molecular mass of 55,810 Da (monomer, calculated molecular mass = 54,419 Da (35)) and a dissociation constant of 33 μM (Fig. 9*D*). These data demonstrate that HsBBS9$_{405-887}$ dimerizes in solution.

We went on to assess whether the N-terminal domain and C-terminal half of HsBBS9 bind to each other. HsBBS9$_{1-407}$ and HsBBS9$_{405-887}$ were mixed in a 1:1 molar ratio prior to SEC in conditions of increasing ionic strength (100 mM NaCl, 10% v/v glycerol; 150 mM NaCl; 500 mM NaCl). Binding was not observed under any of these conditions (Fig. 10, *A* and *B*). This indicates that the HsBBS9 N-terminal β-propeller is flexibly tethered to the C-terminal half of the protein. Based on this series of experiments, we can conclude that HsBBS9$_{1-407}$ dimerization is a crystallization artifact.

Discussion

Here we analyzed the structural and biophysical properties of BBS9, a component of the octameric BBSome. We show that the N-terminal domain folds into a regular β-propeller. How does this information help in deducing the function of BBS9? The protein acts in the context of the octameric BBSome, which forms a membrane coat to select membrane-inserted cargo destined for the primary cilium. The cell has several such membrane coating systems, like COPI, COPII, clathrin and, more distantly related, the nuclear pore complex (36). The architecture of these assemblies is principally related, presumably because of a common evolutionary past (37, 38). Many of the architectural components within these coats are β-propellers, α-helical stacks, or a combination of both. However, the ways in which these elements come together to form the various coats seem to be quite diverse (39–41). Regarding BBS9, our data indicate that it is possibly involved in the higher-order assembly of a BBSome coat. We observed that the protein has a dimerization interface in its C-terminal half. In the context of building a BBSome coat, weak interactions, such as this, might work in an additive manner to build the polymerized assembly. Weak interactions could have evolved such that only small perturbations are required to shift the equilibrium between net polymerization and depolymerization.

In this context, the conserved negative patch on the BBS9 β-propeller domain is particularly intriguing. It is suggestive to propose that it forms a platform for a charge interaction with a peptide or protein of positive character. Other seven-bladed β-propellers are known to bind to positively charged peptides via their negatively charged pores. Examples include β′ COP, a COPI vesicle coat component, which binds endoplasmic reticulum retrieval motifs on cargo proteins (42), and the nucleosome-remodeling factor Nurf55, which binds to the positively charged N terminus of histone H3 via a negatively charged pore (43). Such an electrostatic interaction could be blocked easily by phosphorylation of the binding partner or selective interaction with phospholipids.

Our data indicate that the pathogenic G141R mutation in HsBBS9 likely causes misfolding of the β-propeller domain, which presumably abrogates any potential protein-protein

interaction. Whether this interaction is within the BBSome octamer, or with a neighboring unit in the coat or even an external factor such as cargo, still needs to be understood.

Author Contributions—T. U. S. conceived the study. K. E. K. and T. U. S. designed the experiments, analyzed the data, and wrote the manuscript. K. E. K. performed the experiments.

Acknowledgments—We thank R. Saxton for performing the HEK 293T transient transfection and subsequent Western blot, N. Leksa for experimental advice, S. Bilokapic for help with crystal fishing, and E. Spooner for performing the LC-MS/MS. The x-ray crystallography work was conducted at the Advanced Photon Source (APS) NE-CAT beamlines, which are supported by award GM103403 from the NIGMS, National Institutes of Health. Use of the APS is supported by the Department of Energy, Office of Basic Energy Sciences, under Contract DE-AC02-06CH11357. The Biophysical Instrumentation Facility for the Study of Complex Macromolecular Systems (NSF-007031) is gratefully acknowledged.

References

1. Nachury, M. V., Seeley, E. S., and Jin, H. (2010) Trafficking to the ciliary membrane: how to get across the periciliary diffusion barrier? *Annu. Rev. Cell Dev. Biol.* **26,** 59–87
2. Singla, V., and Reiter, J. F. (2006) The primary cilium as the cell's antenna: signaling at a sensory organelle. *Science* **313,** 629–633
3. Corbit, K. C., Aanstad, P., Singla, V., Norman, A. R., Stainier, D. Y. R., and Reiter, J. F. (2005) Vertebrate Smoothened functions at the primary cilium. *Nature* **437,** 1018–1021
4. Hu, Q., Milenkovic, L., Jin, H., Scott, M. P., Nachury, M. V., Spiliotis, E. T., and Nelson, W. J. (2010) A septin diffusion barrier at the base of the primary cilium maintains ciliary membrane protein distribution. *Science* **329,** 436–439
5. Chih, B., Liu, P., Chinn, Y., Chalouni, C., Komuves, L. G., Hass, P. E., Sandoval, W., and Peterson, A. S. (2012) A ciliopathy complex at the transition zone protects the cilia as a privileged membrane domain. *Nat. Cell Biol.* **14,** 61–72
6. Nachury, M. V., Loktev, A. V., Zhang, Q., Westlake, C. J., Peränen, J., Merdes, A., Slusarski, D. C., Scheller, R. H., Bazan, J. F., Sheffield, V. C., and Jackson, P. K. (2007) A core complex of bbs proteins cooperates with the GTPase Rab8 to promote ciliary membrane biogenesis. *Cell* **129,** 1201–1213
7. Loktev, A. V., Zhang, Q., Beck, J. S., Searby, C. C., Scheetz, T. E., Bazan, J. F., Slusarski, D. C., Sheffield, V. C., Jackson, P. K., and Nachury, M. V. (2008) A BBSome subunit links ciliogenesis, microtubule stability, and acetylation. *Dev. Cell* **15,** 854–865
8. Tobin, J. L., and Beales, P. L. (2009) The nonmotile ciliopathies. *Genet Med.* **11,** 386–402
9. Berbari, N. F., Lewis, J. S., Bishop, G. A., Askwith, C. C., and Mykytyn, K. (2008) Bardet-Biedl syndrome proteins are required for the localization of G protein-coupled receptors to primary cilia. *Proc. Natl. Acad. Sci. U.S.A.* **105,** 4242–4246
10. Jin, H., White, S. R., Shida, T., Schulz, S., Aguiar, M., Gygi, S. P., Bazan, J. F., and Nachury, M. V. (2010) The conserved Bardet-Biedl syndrome proteins assemble a coat that traffics membrane proteins to cilia. *Cell* **141,** 1208–1219
11. Wei, Q., Zhang, Y., Li, Y., Zhang, Q., Ling, K., and Hu, J. (2012) The BBSome controls IFT assembly and turnaround in cilia. *Nat. Cell Biol.* **14,** 950–957
12. Mourão, A., Nager, A. R., Nachury, M. V., and Lorentzen, E. (2014) Structural basis for membrane targeting of the BBSome by ARL6. *Nat. Struct. Mol. Biol.* **21,** 1035–1041
13. Nishimura, D. Y., Swiderski, R. E., Searby, C. C., Berg, E. M., Ferguson, A. L., Hennekam, R., Merin, S., Weleber, R. G., Biesecker, L. G., Stone, E. M., and Sheffield, V. C. (2005) Comparative genomics and gene expression analysis identifies *BBS9*, a new Bardet-Biedl syndrome gene. *Am. J. Hum. Genet.* **77,** 1021–1033
14. Veleri, S., Bishop, K., Dalle Nogare, D. E., English, M. A., Foskett, T. J., Chitnis, A., Sood, R., Liu, P., and Swaroop, A. (2012) Knockdown of Bardet-Biedl syndrome gene *BBS9/PTHB1* leads to cilia defects. *PLoS ONE* **7,** e34389
15. Andersen, K. R., Leksa, N. C., and Schwartz, T. U. (2013) Optimized *E. coli* expression strain LOBSTR eliminates common contaminants from His-tag purification. *Proteins* **81,** 1857–1861
16. Brohawn, S. G., Leksa, N. C., Spear, E. D., Rajashankar, K. R., and Schwartz, T. U. (2008) Structural evidence for common ancestry of the nuclear pore complex and vesicle coats. *Science* **322,** 1369–1373
17. Otwinowski, Z., and Minor, W. (1997) Processing of x-ray diffraction data collected in oscillation mode. *Method Enzymol.* **276,** 307–326
18. Adams, P. D., Afonine, P. V., Bunkóczi, G., Chen, V. B., Davis, I. W., Echols, N., Headd, J. J., Hung, L. W., Kapral, G. J., Grosse-Kunstleve, R. W., McCoy, A. J., Moriarty, N. W., Oeffner, R., Read, R. J., Richardson, D. C., Richardson, J. S., Terwilliger, T. C., and Zwart, P. H. (2010) PHENIX: a comprehensive Python-based system for macromolecular structure solution. *Acta Crystallogr. D Biol. Crystallogr.* **66,** 213–221
19. Emsley, P., Lohkamp, B., Scott, W. G., and Cowtan, K. (2010) Features and development of Coot. *Acta Crystallogr. D Biol. Crystallogr.* **66,** 486–501
20. Krissinel, E., and Henrick, K. (2007) Inference of macromolecular assemblies from crystalline state. *J. Mol. Biol.* **372,** 774–797
21. Ashkenazy, H., Erez, E., Martz, E., Pupko, T., and Ben-Tal, N. (2010) ConSurf 2010: calculating evolutionary conservation in sequence and structure of proteins and nucleic acids. *Nucleic Acids Res.* **38,** W529-W533
22. Waterhouse, A. M., Procter, J. B., Martin, D. M. A., Clamp, M., and Barton, G. J. (2009) Jalview Version 2: a multiple sequence alignment editor and analysis workbench. *Bioinformatics* **25,** 1189–1191
23. Altschul, S. F., Gish, W., Miller, W., Myers, E. W., and Lipman, D. J. (1990) Basic local alignment search tool. *J. Mol. Biol.* **215,** 403–410
24. Kelley, L. A., and Sternberg, M. J. E. (2009) Protein structure prediction on the Web: a case study using the Phyre server. *Nat. Protoc.* **4,** 363–371
25. Baker, N. A., Sept, D., Joseph, S., Holst, M. J., and McCammon, J. A. (2001) Electrostatics of nanosystems: application to microtubules and the ribosome. *Proc. Natl. Acad. Sci. U.S.A.* **98,** 10037–10041
26. DeLano, W. L. (2010) *The PyMOL Molecular Graphics System*, version 1.3r1, Schrödinger, LLC, New York
27. Demeler, B. (2005) UltraScan: a comprehensive data analysis software package for analytical ultracentrifugation experiments. in *Modern Analytical Ultracentrifugation: Techniques and Methods*, pp. 210–229, Royal Society of Chemistry, Royal Society of Chemistry, Cambridge, UK, 10.1039/9781847552617-00210
28. Morin, A., Eisenbraun, B., Key, J., Sanschagrin, P. C., Timony, M. A., Ottaviano, M., and Sliz, P. (2013) Collaboration gets the most out of software. *eLife* **2,** e01456
29. Fong, H. K., Hurley, J. B., Hopkins, R. S., Miake-Lye, R., Johnson, M. S., Doolittle, R. F., and Simon, M. I. (1986) Repetitive segmental structure of the transducin β subunit: homology with the *CDC4* gene and identification of related mRNAs. *Proc. Natl. Acad. Sci. U.S.A.* **83,** 2162–2166
30. Wall, M. A., Coleman, D. E., Lee, E., Iñiguez-Lluhi, J. A., Posner, B. A., Gilman, A. G., and Sprang, S. R. (1995) The structure of the G protein heterotrimer $G_i\alpha_1\beta_1\gamma_2$. *Cell* **83,** 1047–1058
31. Xu, C., and Min, J. (2011) Structure and function of WD40 domain proteins. *Protein Cell* **2,** 202–214
32. Holm, L., and Rosenström, P. (2010) Dali server: conservation mapping in 3D. *Nucleic Acids Res.* **38,** W545-W549
33. Heenan, E. J., Vanhooke, J. L., Temple, B. R., Betts, L., Sondek, J. E., and Dohlman, H. G. (2009) Structure and function of Vps15 in the endosomal G protein signaling pathway. *Biochemistry* **48,** 6390–6401
34. Brown, J. T., Bai, X., and Johnson, A. W. (2000) The yeast antiviral proteins Ski2p, Ski3p, and Ski8p exist as a complex *in vivo*. *RNA* **6,** 449–457
35. Wilkins, M. R., Gasteiger, E., Bairoch, A., Sanchez, J. C., Williams, K. L., Appel, R. D., and Hochstrasser, D. F. (1999) Protein identification and analysis tools in the ExPASy server. *Methods Mol. Biol.* **112,** 531–552
36. Brohawn, S. G., Partridge, J. R., Whittle, J. R. R., and Schwartz, T. U. (2009)

The nuclear pore complex has entered the atomic age. *Structure* **17,** 1156–1168
37. Devos, D., Dokudovskaya, S., Alber, F., Williams, R., Chait, B. T., Sali, A., and Rout, M. P. (2004) Components of coated vesicles and nuclear pore complexes share a common molecular architecture. *Plos Biol.* **2,** e380
38. Mans, B. J., Anantharaman, V., Aravind, L., and Koonin, E. V. (2004) Comparative genomics, evolution and origins of the nuclear envelope and nuclear pore complex. *Cell Cycle* **3,** 1612–1637
39. Fotin, A., Cheng, Y., Sliz, P., Grigorieff, N., Harrison, S. C., Kirchhausen, T., and Walz, T. (2004) Molecular model for a complete clathrin lattice from electron cryomicroscopy. *Nature* **432,** 573–579
40. Fath, S., Mancias, J. D., Bi, X., and Goldberg, J. (2007) Structure and organization of coat proteins in the COPII cage. *Cell* **129,** 1325–1336
41. Lee, C., and Goldberg, J. (2010) Structure of coatomer cage proteins and the relationship among COPI, COPII, and clathrin vesicle coats. *Cell* **142,** 123–132
42. Ma, W., and Goldberg, J. (2013) Rules for the recognition of dilysine retrieval motifs by coatomer. *EMBO J.* **32,** 926–937
43. Schmitges, F. W., Prusty, A. B., Faty, M., Stützer, A., Lingaraju, G. M., Aiwazian, J., Sack, R., Hess, D., Li, L., Zhou, S., Bunker, R. D., Wirth, U., Bouwmeester, T., Bauer, A., Ly-Hartig, N., Zhao, K., Chan, H., Gu, J., Gut, H., Fischle, W., Müller, J., and Thomä, N. H. (2011) Histone methylation by PRC2 is inhibited by active chromatin marks. *Mol. Cell* **42,** 330–341
44. Ciccarelli, F. D., Doerks, T., von Mering, C., Creevey, C. J., Snel, B., and Bork, P. (2006) Toward automatic reconstruction of a highly resolved tree of life. *Science* **311,** 1283–1287
45. Fritz-Laylin, L. K., Prochnik, S. E., Ginger, M. L., Dacks, J. B., Carpenter, M. L., Field, M. C., Kuo, A., Paredez, A., Chapman, J., Pham, J., Shu, S., Neupane, R., Cipriano, M., Mancuso, J., Tu, H., Salamov, A., Lindquist, E., Shapiro, H., Lucas, S., Grigoriev, I. V., Cande, W. Z., Fulton, C., Rokhsar, D. S., and Dawson, S. C. (2010) The genome of *Naegleria gruberi* illuminates early eukaryotic versatility. *Cell* **140,** 631–642